JOURNAL OF GEOPHYSICAL RESEARCH, VOL. 102, NO. B10, PAGES 22,749–22,764, OCTOBER 10, 1997

A numerical study of anisotropic, low Reynolds number, free surface flow for ice sheet modeling

Anne Mangeney[1,2]

Laboratoire de Glaciologie et Geophysique de l'Environnement, CNRS, Saint Martin d'Heres France

Francesco Califano[1]

Scuola Normale Superiore, Pisa, Italy

Kolumban Hutter

Institut für Mechanik, Technische Hochschule, Darmstadt, Germany

Abstract. Few ice sheet flow models have been developed that solve the complete set of mechanical equations. Until now, these models were limited to isotropic conditions. We present here a two-dimensional, finite difference method capable of solving the equations for the steady flow of a viscous, incompressible, anisotropic fluid with a free surface under isothermal conditions. It is not a standard method, especially with respect to the time discretization of the numerical scheme, and converges for very low Reynolds numbers. This method is applied here to the planar flow of anisotropic ice over flat or irregular bedrock, with no-slip boundary conditions at the ice-bedrock interface. The results are presented here for Newtonian behavior in the vicinity of an ice divide. The ice is assumed to be isotropic at the ice sheet surface, with continuous and prescribed development of anisotropy with increasing depth. Going from isotropic to anisotropic situations, our results indicate that the free surface becomes flatter and the shear strain rates larger and more concentrated near the bedrock. The flow is less sensitive to variations of the bedrock topography in the anisotropic case than in the isotropic case. Furthermore, a new phenomenon appears in the anisotropic case: the partial stagnation of ice in the holes of the bedrock. These effects have significant consequences when dating the ice. The isochrones obtained in the anisotropic case are flatter and the anisotropic ice is more than 10% younger above the bumps and more than 100% older within the holes than for the isotropic ice.

1. Introduction

Ice sheet flow models generally use the shallow ice approximation [*Hutter et al.*, 1981; *Fowler and Larson*, 1980; *Hutter*, 1993], based on the existence of a small aspect ratio. This approximation significantly simplifies the mechanical equations but the limits of its application were clearly defined only very recently (A. Mangeney and F. Califano, The shallow-ice approximation for anisotropic ice: Formulation and limits, submitted to *Journal of Geophysical Research*, 1997, hereinafter referred to as Mangeney and Califano, submitted manuscript, 1997). Furthermore, we must remember that the shallow ice approximation was not developed for anisotropic ice. The study of the effects of anisotropy on ice sheet flow requires then the use of a numerical model capable of solving the complete set of mechanical equations. Only a handful of numerical models have been developed so far. They use the finite element method and solve the complete set of mechanical equations for isotropic ice [*Raymond*, 1983; *Paterson and Waddington*, 1984; *Firestone et al.*, 1990; *Schott Hvidberg*, 1993, 1996].

We present here the first finite difference model able to solve the complete set of mechanical equations for the anisotropic case. As a first approach, we simplify our study by assuming two-dimensional (2-D), isothermal, and steady state conditions. We neglect here the special problem of margin evolution by restricting our-

[1] Also at Observatoire de Paris-Meudon (DESPA), Meudon, France.

[2] Now at Institut de Physique du Globe de Paris, Paris, France.

Paper number 97JB01697.
0148-0227/97/97JB-01697$09.00

selves to interior domains. We solve the Navier-Stokes equations within a bounded domain Ω of boundary Γ in the vicinity of the center of the ice sheet (i.e., ice divide). The horizontal length of the domain is fixed, and horizontal velocities are imposed at the right and left sides. Our calculations show that when the boundaries are sufficiently far from the center, there exists a region around the ice divide where the solution is insensitive to the boundary conditions. These results are in agreement with those of *Raymond* [1983].

The numerical method is derived from methods that were constructed to treat incompressible transient flows. It is not a standard method, especially with regard to the time discretization of the numerical scheme. To solve the steady state, anisotropic flow problem, we introduce a fictitious time derivative of the velocity into the momentum equation, and we let the surface evolve until a steady state is reached for both the surface elevation and the velocity field. In the method used here (very similar to the projection method), the continuity equation is replaced by an elliptic Poisson equation for the pressure. The Dirichlet boundary conditions for the velocity at the right and left edges of the domain and the no-slip condition at the base of the ice sheet are replaced by Neumann conditions for the pressure. Two major difficulties appear in the numerical treatment. The first concerns the temporal discretization of the numerical scheme for low Reynolds number flows. The second difficulty is related to the spatial discretization which must be such that (1) the discretized form of the continuity equation is satisfied to a sufficient degree of accuracy and (2) the discrete compatibility condition for the Poisson-Neumann problem for the pressure holds.

It is well known in glaciology that the geometry of the domain evolves on a characteristic timescale that is much shorter than that of the velocity and strain rate field variations [see, e.g., *Hutter*, 1993]. Therefore it is possible to decouple the calculation of the surface evolution and that of the mechanical equilibrium. The surface evolution is calculated only to conform with a fixed accumulation rate. We introduce a system of reduced coordinates that leads to substantial simplification in the treatment of the boundary conditions at the free surface.

The numerical code takes into account the anisotropy of the material. Mechanical tests in laboratory and strain rate measurements in ice sheets have shown that the surface ice has an isotropic structure, while the deformation of deep ice strongly depends on the direction of the applied stress. This viscoplastic anisotropy results from a preferred orientation of the crystallographic planes of the ice crystals (texture) observed in deep polar ices. The texture of polar ice is known to be a function of the thermomechanical history of ice particles along their trajectories in the ice sheet. It is not simple to take into account the anisotropic behavior of the ice because this necessitates the use of an anisotropic flow law that correctly describes the ice behavior under large deformation and that is easy to integrate in a flow model. A realistic flow law should calculate the response of the ice polycrystal for a given texture as a function of the imposed stress or strain rate as well as the evolution of the texture with the thermomechanical history of the material. Such a law may be obtained numerically with homogenization methods [*Van der Veen and Whillans*, 1994; *Azuma*, 1994; *Castelnau et al.*, 1996; *Castelnau*, 1996]. However, these methods are able to calculate the texture development observed in ice sheets only when the recrystallization mechanisms, presently poorly understood, are taken into account [*Castelnau*, 1996]. Furthermore, the introduction of such a law into a flow model results in high computational costs [*Beaudoin et al.*, 1994]. On the other hand, analytical flow laws, even if more limited in the physical representation of the deformation mechanisms, have the advantage of being simple to introduce into large-scale flow models [*Lliboutry*, 1993; *Svendsen and Hutter*, 1996]. Up until now, no analytical flow law, useful in a flow model and capable of calculating the evolution of the texture and the associated rheology, is available. For this reason, we introduce the anisotropy in a simple way by using an anisotropic flow law that does not take into account the evolution of the texture with the thermomechanical history [*Lliboutry*, 1993]. Lliboutry's model gives a good approximation of the ice anisotropic behavior, although it underestimates ice anisotropy [*Castelnau et al.*, 1997].

The mechanical behavior of the isotropic ice is generally described by the classical Norton-Hoff constitutive relation called Glen's flow law in glaciology [*Nye*, 1957]. For isotropic ice, *Lliboutry*'s [1993] anisotropic flow law is equivalent to Glen's flow law. The exponent n of this power law is not accurately known [*Hooke*, 1981]. Even though a value of $n = 3$ is generally accepted for effective stresses larger than 0.2 MPa, a value of n lower than 2 seems to be more appropriate for effective stresses lower than approximately 0.2 MPa [*Doake and Wolff*, 1985; *Pimienta and Duval*, 1987; *Alley*, 1992]. The anisotropic flow law of Lliboutry assumes such Newtonian behavior at low stresses. We will limit the study here to Newtonian behavior of the ice.

Results on the effects of anisotropy on the Newtonian flow over a flat bedrock for a fixed geometry have been discussed previously [*Mangeney et al.*, 1996]. We will present here what happens for a more realistic case, when the free surface evolves in order to adjust to a fixed accumulation rate and when perturbations of the bedrock topograpy are introduced.

This paper is structured as follows: we first give the equations of the model, then a description of the numerical method for solving the complete set of equations, and, finally, the results of the effects of anisotropy on the ice flow over a flat and irregular bedrock.

Table 1. Simulation Parameters

	Description
	Physical Parameters
$\rho = 900$ kg m^{-3}	ice density
$g = 9.81$ m s^{-2}	acceleration due to gravity
$Q = 7.820 \times 10^4$ J mol^{-1}	activation energy
$R = 8.314$ J mol^{-1} K^{-1}	gas constant
	Scaling Values
$u_* = 0.2$ m yr^{-1}	typical vertical velocity or accumulation rate
$d_* = 2500$ m	representative thickness

2. Equations

2.1. Mechanical Equations

The evolution of an anisotropic, viscoplastic, isothermal ice sheet can be studied by solving the equations of conservation of mass and momentum coupled with a constitutive relation for the stress tensor. We choose the thickness d_* of the ice sheet as a characteristic length and the accumulation rate u_* as a characteristic velocity. The dimensional characteristic stress is then given by $\tau_* = \varrho g d_*$ (here ϱ is the density and g is the acceleration due to gravity), which corresponds to the hydrostatic pressure at the base of the ice sheet (see Table 1 for numerical values). Then, the nondimensional equations read

$$\nabla.\mathbf{u} = 0, \tag{1}$$

$$\nabla.\mathbf{S}' = \nabla p', \tag{2}$$

where $\mathbf{u}=(u_x, u_z)$ is the velocity vector, $p' = p - z$ is the dynamic pressure, p is the fluid pressure, and $\mathbf{S}'$ is the Cauchy stress tensor given by

$$\mathbf{S}' = \sigma + p\mathbf{I}, \quad p = -\frac{1}{3}\mathrm{tr}(\sigma).$$

where σ is the stress tensor, $\mathbf{I}$ is the identity tensor, and tr is the trace operator. Notice that owing to the very low velocities (for which typical Reynolds numbers are of the order of $\sim 10^{-10}$), the inertia terms in the equation of motion (2) can be neglected.

2.2. Constitutive Relation

The conservation equations (1) and (2) are solved together with the constitutive relation of the ice:

$$\mathbf{S}' = \mathbf{M} : \mathbf{D}, \tag{3}$$

where $\mathbf{M}$ and $\mathbf{D}$ are the fourth-order viscosity tensor and the second-order strain rate tensor, normalized by $\tau_* d_*/u_*$ and u_*/d_*, respectively. The constitutive relation used here is that of *Lliboutry* [1993], which gives the viscoplastic anisotropic response of the ice for a fixed texture.

The texture is assumed to be a function of the reduced depth $\overline{z} = (z - B)/H$ ($H = E - B$ is the ice thickness) only; that is, it is invariant along the x direction and it does not depend on the deformation history of the ice. Texture development with reduced depth was fitted on the fabric data of the recent GReenland Ice core Project (GRIP) ice core [*Thorsteinsson et al.*, 1997], which represents a typical texture distribution for ice sheets (Figure 1a). The texture is randomly oriented at the surface, and the ice is then isotropic. Deeper down, the ice crystals strongly concentrate around the vertical in situ direction (single maximum texture). As a consequence, the ice easily deforms when subjected to horizontal shear, but it strongly resists all longitudinal stresses. The rheological parameters used here are those determined by *Mangeney et al.* [1996]. In this case, for a planar flow the constitutive relation (3) takes the form

$$\begin{bmatrix} S'_{xx} \\ S'_{yy} \\ S'_{zz} \\ S'_{xz} \end{bmatrix} = \begin{bmatrix} \eta_{11} & \eta_{12} & \eta_{13} & 0 \\ \eta_{12} & \eta_{22} & \eta_{23} & 0 \\ \eta_{13} & \eta_{23} & \eta_{33} & 0 \\ 0 & 0 & 0 & \eta_{44} \end{bmatrix} \begin{bmatrix} D_{xx} \\ D_{yy} \\ D_{zz} \\ D_{xz} \end{bmatrix} \tag{4}$$

where η_{ij} are functions of the texture and of the deviatoric stresses when non-Newtonian flow is considered [*Mangeney et al.*, 1996]. The dependence of the viscosity matrix components η_{ij} on the four invariants of the deviatoric stress tensor is given by *Lliboutry* [1993] and *Mangeney et al.* [1996]. As a result, in the Newtonian case, for strongly textured, anisotropic ice near the bottom, the shear strain rate in response to a shear stress is more than 1 order of magnitude larger than the longitudinal strain rate in response to a longitudinal stress for the same absolute value of the applied stress (Figure 1b). At the surface (isotropic ice), this constitutive relation (3) is reduced to the generalized Glen's flow law with a Newtonian and a non-Newtonian term [*Mangeney*, 1996; Mangeney and Califano, submitted manuscript, 1997]:

$$D_{ij} = \left(A_3\tau^2 + A_1\right) S'_{ij}, \tag{5}$$

where A_n is the temperature-dependent rate factor:

$$A_n = A_n^0 \exp(-Q/RT), \tag{6}$$

and τ is the effective stress defined as

$$\tau^2 = \frac{1}{2}\mathrm{tr}(\mathbf{S}'^2) \tag{7}$$

where n is the stress sensitivity, Q is the activation energy for creep, R is the gas constant, and T is the absolute temperature. In this work we consider a Newtonian flow ($A_3 = 0$) and we impose an ice temperature of $-20°$C and the value of $A_1 = 2.8 \times 10^3$ [*Duval and Castelnau*, 1995] (A_1 is normalized by $u_*/(\tau_* d_*)$) This flow law is discussed in more detail by *Mangeney et al.* [1996] and *Mangeney* [1996].

2.3. Boundary Conditions

The ice sheet flow is studied in the framework of a 2-D slab geometry, where the x and z axes refer to the horizontal and vertical directions, respectively. The

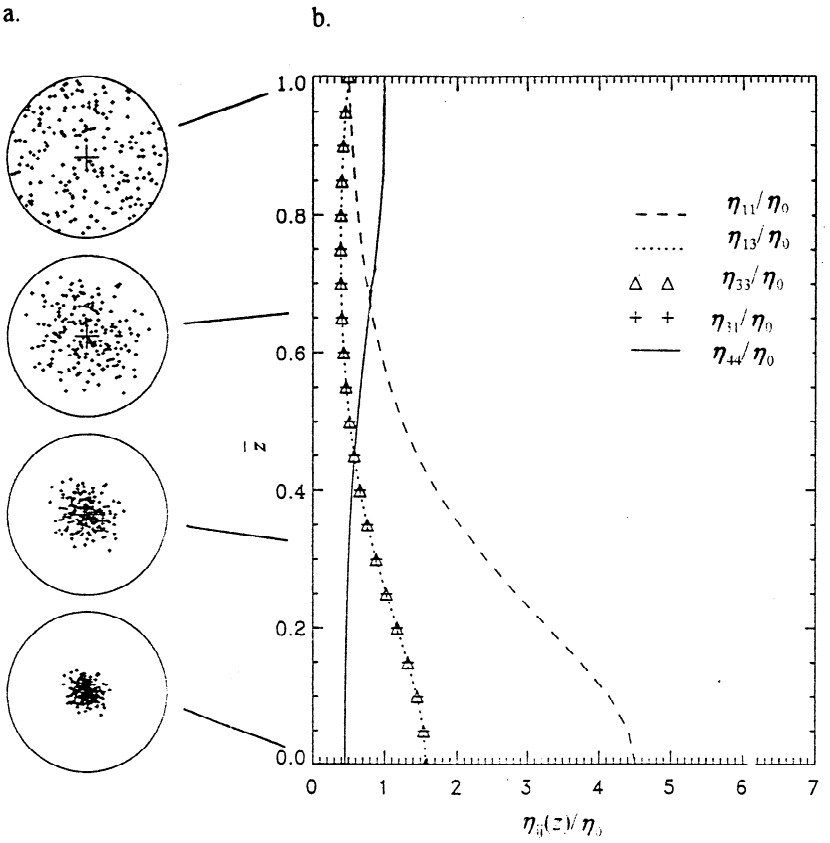

Figure 1. Characteristic of the fabric used in the model and the associated directional viscosities. (a) Development of the texture at 0, 1/4, 1/2, 3/4, and 1 times the depth. (b) Components of the viscosity matrix resulting from this texture. The viscosity tensor components η are denoted by symbols.

plane (x, z) is a symmetry plane for the flow (that is $\partial/\partial y = 0$), with an aspect ratio equal to the inverse of the horizontal length $L = 40$.

The kinematic condition at the free surface $z = E(x)$ is given by

$$\frac{\partial E}{\partial t} + u_x \frac{\partial E}{\partial x} - u_z = a, \tag{8}$$

where a is the accumulation rate. If p_{atm} is the atmospheric pressure and $\mathbf{n}_s$ is the exterior unit normal vector at the surface, the stress free, top surface condition reads

$$\sigma.\mathbf{n}_s - p_{\text{atm}}\mathbf{n}_s = 0 \tag{9}$$

At the base of the ice sheet we consider an uneven, sinusoidal bedrock $B(x)$, where the fluid is assumed to be at rest $[\mathbf{u}(x, z = B(x)) = \mathbf{0})]$, with typical irregularities characterized by a wavenumber f and an amplitude B_0:

$$B(x) = B_0 \cos\left[2\pi f \frac{x}{L}\right]. \tag{10}$$

At the left-hand and right-hand side of the domain we impose the velocity profiles given by *Nye* [1952] corresponding to "laminar" flow and satisfying the mass balance condition [see *Mangeney et al.*, 1996]. However, we find that the flow inside the domain of integration is independent of the left/right boundary conditions, except close to the boundaries, where boundary layers develop. In these layers, when the boundary conditions are not realistic, strong horizontal pressure gradients appear. On the other hand, at the top and bottom surfaces the boundary conditions fit the real flow exactly.

3. Numerical Method

We shall first illustrate the numerical method used to solve the system of equations (1)-(3); we will then consider separately the specific treatment of the free surface. Numerical solution schemes of the steady, incompressible Navier-Stokes equations have been studied in great detail. A possible approach is the so-called artificial compressibility method, where a new term (a time derivative of the pressure) is introduced in the continuity equation [*Chorin*, 1967]. This term is a numerical artifact, and the solution has physical significance only when the stationary state is reached.

A more general approach is to solve the unsteady Navier-Stokes equations, allowing the system to relax until a steady state is reached. These methods have been widely explored since they can be implemented also when one is interested in time-dependent solutions. In this case the procedure generally leads to the replacement of the continuity equation (1) by an elliptic pressure Poisson equation obtained from divergence of the equation of motion (2). The Dirichlet boundary condi-

tions for the velocities at the boundaries of the domain are replaced by Neumann conditions for the pressure field.

3.1. Time Scheme

To solve numerically the system of equations (1)-(3), we reintroduce the time derivative of the velocity in the momentum equation,

$$\frac{\partial \mathbf{u}}{\partial t} = \mathcal{L}\mathbf{u} - \nabla p', \qquad \nabla \cdot \mathbf{u} = 0, \tag{11}$$

where $\mathcal{L}$ is a second-order differential operator, and let the system evolve until a steady state is reached.

Since ice sheet flows are characterized by very low Reynolds numbers, it is necessary to use an implicit, time-advancing scheme in order to limit computational costs in achieving the solution at the required accuracy [*Pracht*, 1971]. In our case we find that when only the diagonal part $\mathcal{L}_d$ of the operator $\mathcal{L}$ ($\mathcal{L} = \mathcal{L}_d + \delta\mathcal{L}$) is implicit, it provides a good compromise between stability and computational costs. Such a "semi-implicit" scheme requires minor modifications with respect to the explicit scheme, which diverges for low Reynolds number flows.

Adopting the projection method [*Peyret and Taylor*, 1983], we first calculate an intermediate velocity field at time step m,

$$\hat{\mathbf{u}} = \frac{\alpha^+}{\alpha^-}\mathbf{u}^{(m)} + \frac{\Delta t}{\alpha^-}\delta\mathcal{L}\mathbf{u}^{(m)}, \quad \alpha^{\pm} = 1 \pm \Delta t\mathcal{L}_d/2. \tag{12}$$

The actual velocity field at time step $m+1$ is given by

$$\mathbf{u}^{(m+1)} = \hat{\mathbf{u}} - \gamma\nabla p'^{(m+1)}, \quad \gamma = \frac{\Delta t}{\alpha^-}, \tag{13}$$

Here the pressure $p'^{(m+1)}$ is determined by solving the Poisson equation

$$(\nabla\gamma)\,\nabla p'^{(m+1)} + \gamma\nabla^2 p'^{(m+1)} = \nabla \cdot \hat{\mathbf{u}}, \tag{14}$$

which is obtained by imposing $\nabla \cdot \mathbf{u}^{(m+1)} = 0$ in (13). The boundary conditions for p' are obtained by taking the scalar product of (13) with the normal vector $\mathbf{n}$ at the boundary Γ:

$$\left(\frac{\partial p'}{\partial n}\right)_{\Gamma}^{(m+1)} = -\frac{1}{\gamma_n}\left(\mathbf{u}_{\Gamma}^{(m+1)} - \hat{\mathbf{u}}_{\Gamma}\right).\mathbf{n}, \tag{15}$$

where γ_n is the projection of γ on $\mathbf{n}$ and $\hat{\mathbf{u}}_{\Gamma}$ is the value of $\hat{\mathbf{u}}$ on Γ, which must satisfy the compatibility condition for the Poisson-Neumann problem, relating the source term of the Poisson equation to the Neumann boundary conditions (Green theorem) [*Fortin et al.*, 1971]. This condition reads, in the explicit case,

$$\frac{1}{\Delta t}\int_{\Omega} \nabla.\hat{\mathbf{u}}d\Omega = -\frac{1}{\Delta t}\int_{\Gamma}\left(\mathbf{u}^{(m+1)} - \hat{\mathbf{u}}\right).\mathbf{n}d\Gamma \tag{16}$$

and is identically satisfied since the velocity $\mathbf{u}^{(m+1)}$ has a total flux equal to zero on Γ. The choice of the spatial discretization must satisfy the discrete analogue of (16). Note that since the coefficient γ, which is directly related to the viscosity tensor, is not constant on the domain of integration, pressure gradients appear in the Poisson equation (14).

3.2. Spatial Discretization

The main difficulties related to the spatial discretization of (12)-(14) are (1) ensuring the free divergence of the flow at a satisfactory accuracy, (2) satisfying the compatibility condition, and, finally, (3) avoiding numerical grid oscillations on the pressure field.

The two most frequently used schemes are the projection and the marker and cell (MAC) methods [see *Peyret and Taylor* [1983], and references therein]. In the first the pressure equation is obtained and then discretized, while in the second the pressure equation is obtained by the discretized divergence of the discretized momentum equation. The Poisson equations given by the two different methods coincide when a staggered grid is used. In this case all the previous requirements are satisfied, but such a grid requires a large amount of computer memory and introduces a high level of algebraic complexity. These two disadvantages can be avoided by using a nonstaggered (i.e., collocated) grid, where all the fields are calculated at the same points, but as a consequence, the three conditions, (1), (2), and (3), are not automatically satisfied. In this case the discretized pressure equations obtained with the projection or MAC methods are different. In particular, for the MAC method the discretized continuity equation is satisfied to within the round-off error of the machine, but the odd-even decoupling leads to numerical oscillations of the pressure field [*Sotiropoulos and Abdallah*, 1991]. For this reason, we have followed the projection method

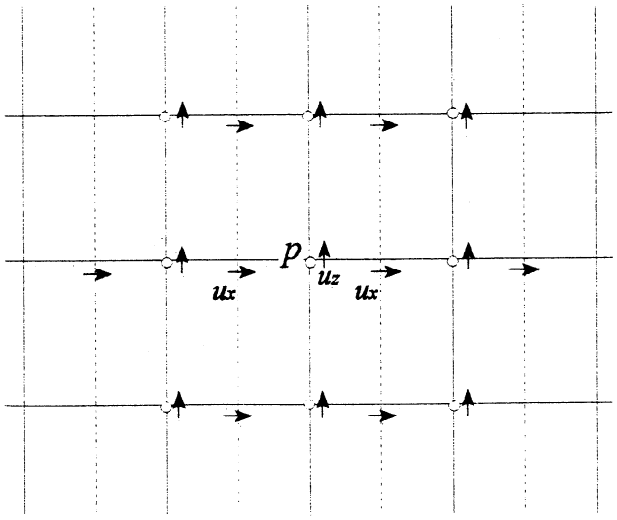

Figure 2. Semistaggered grid. Major meshes are represented by solid lines, and minor meshes are represented by dotted lines.

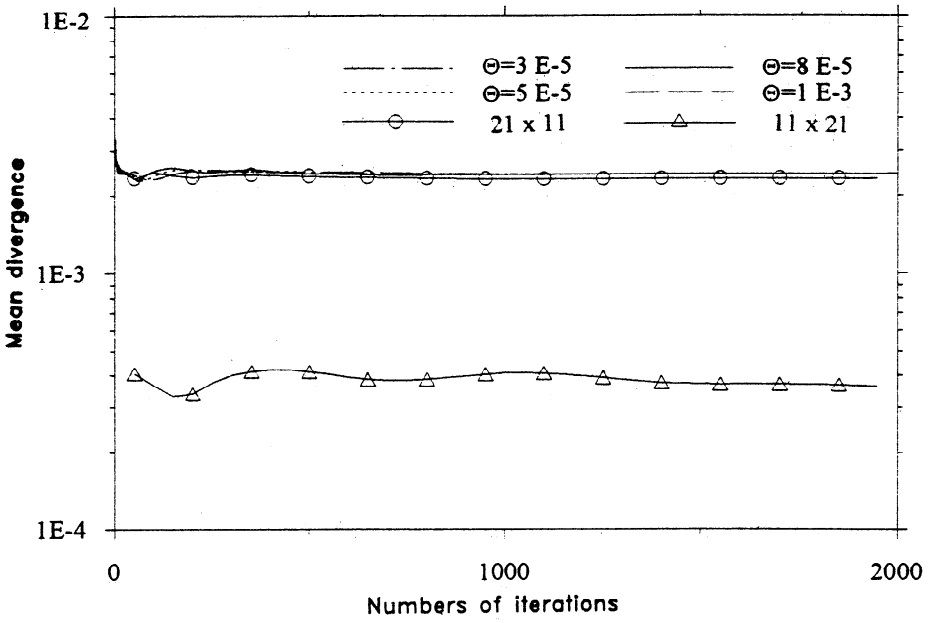

Figure 3. Mean divergence of the velocities for different time steps Θ as a function of the iteration number for $(N_x, N_z) = (11 \times 11)$ points. N_x and N_z represent the number of horizontal and vertical points, respectively. The mean divergence is also represented by circles for (21×11) points and by triangles for (11×21) points for $\Theta = 2.5 \times 10^{-5}$; Θ may vary from 0 to 1 and is defined as $\Theta = \max(\mathcal{L}_d)\Delta t/2$

for which numerical oscillations of the pressure are easily avoided by an appropriate discretization [*Abdallah*, 1987a, b], even if the incompressibility and compatibility conditions, 1 and 2, respectively, must be carefully considered. Note that use of a collocated grid leads to a numerical mass source for the discretized continuity equation that is proportional essentially to the fourth-order derivative of the pressure [*Sotiropoulos and Abdallah*, 1991].

As discussed in section 2.3, strong, horizontal, spatial gradients develop close to the left and right boundaries. These strong gradients are an important source of numerical error for the incompressibility condition. Therefore we implemented a staggered horizontal grid, while in the vertical direction we used a collocated grid (see Figure 2). With this grid the numerical error on the discretized continuity equation is essentially proportional to the vertical fourth-order derivative of the pressure and to the space step squared [*Sotiropoulos and Abdallah*, 1991]. It is then possible to lower this error by taking more points in the vertical direction. The precision of the value of the mean divergence of the velocities within the numerical domain is improved by about 1 order of magnitude when we take 21 points in the vertical direction instead of 11 points (see Figure 3).

The Poisson equation (14) is solved on the entire numerical grid, except at the top boundary, where the free surface condition is imposed (see section 3.3). Therefore two vertical and one horizontal, external, fictitious meshes are added at the left, right, and bottom boundaries, respectively, allowing us to impose the boundary conditions on the pressure.

While in the horizontal direction the compatibility condition is automatically satisfied, in the vertical direction the gradient of the pressure must be calculated at the middle of two points and averaged on the collocated grid [*Abdallah*, 1987a, b]. The discretized form of (14) reads

$$\left(\frac{\gamma_{x\,i+1,j} - \gamma_{x\,i,j}}{\Delta x}\right)\left(\frac{p_{i+1,j}^{(m+1)} - p_{i-1,j}^{(m+1)}}{2\Delta x}\right) + \left(\frac{\gamma_{z\,i,j+1} - \gamma_{z\,i,j-1}}{2\Delta z}\right)\left(\frac{p_{i,j+1}^{(m+1)} - p_{i,j-1}^{(m+1)}}{2\Delta z}\right) + \bar{\gamma}_{x\,i,j}\left(\frac{p_{i+1,j}^{(m+1)} - 2p_{i,j}^{(m+1)} - p_{i-1,j}^{(m+1)}}{(\Delta x)^2}\right) + \gamma_{z\,i,j}\left(\frac{p_{i,j+1}^{(m+1)} - 2p_{i,j}^{(m+1)} - p_{i,j-1}^{(m+1)}}{(\Delta z)^2}\right) = \frac{\hat{u}_{x\,i+1,j} - \hat{u}_{x\,i,j}}{\Delta x} + \frac{\hat{u}_{z\,i,j+1} - \hat{u}_{z\,i,j-1}}{2\Delta z}, \quad (17)$$

where γ_x and γ_z represent the projections of γ into the horizontal and vertical direction, respectively, and $\bar{\gamma}_x$ is the value of γ_x on the major mesh, obtained by calculating the arithmetic average of the values of γ_x on the two adjacent minor mesh points (see Figure 2).

The presence of pressure gradients in the Poisson equation (14) complicates the imposing of the boundary condition in order to satisfy the compatibility condition. Following the discretized form of the pressure gradient used in the Poisson equation, we impose the Neumann boundary conditions at the left ($i = 1$) and

right ($i = N_x$) boundaries as follows

$$\frac{p_{i+1,j}^{(m+1)} - p_{i-1,j}^{(m+1)}}{2\Delta x} = \frac{1}{\bar{\gamma}_x}\left(\hat{u}_{x\,i,j} - u_{x\,i,j}^{m+1}\right). \quad (18)$$

At the bottom boundary ($j = N_z$) the same condition reads

$$\frac{p_{i,j+1}^{(m+1)} - p_{i,j-1}^{(m+1)}}{2\Delta z} = \frac{1}{\gamma_z}\left(\hat{u}_{z\,i,j} - u_{z\,i,j}^{m+1}\right). \quad (19)$$

We found, using these conditions, that the numerical code converges with the required accuracy for all the cases treated. It is worthwile to emphasize that, in the case of an implicit treatment, it is necessary to impose the values of the velocity at time step $m+1$ (instead of m) on the right-hand side of (18) and (19). A detailed numerical study of the convergence and the accuracy of the code is presented by *Mangeney* [1996].

3.3. Free Surface

When the upper boundary of the domain is characterized by the presence of a free surface, the MAC method has been primarily used. In this method the equations are solved in a fixed Eulerian grid, and a different reference frame follows the particle's trajectories, giving the position of the free surface [*Harlow and Welch*, 1965; *Pracht*, 1971; *Deville*, 1975]. Unfortunately, the free surface is not exactly localized, in general, on the numerical grid. As a result, it is difficult to impose the surface boundary conditions. An alternative approach is to use Lagrangian methods, which require frequent reinitializations of all the physical fields leading to a lower numerical accuracy at larger computational costs [*Morton*, 1971].

In our case we use a rather different method that allows us to fit the numerical grid on the ice sheet geometry at each time step by using a coordinate transformation [*Phillips*, 1957; *Jenssen*, 1977; *Hindmarsh and Hutter*, 1988]. The physical, irregular domain in the plane (x, z) is transformed into a regular (rectangular), time-independent domain in the (ζ, ξ) space. This easier and less expensive method can be used since in our problem the free surface is not subjected to very complicated phenomena such as wave breaking, for instance. Actually, assuming that the ice sheet has a fixed horizontal length, the variable transformation is limited to the vertical direction and is given by

$$\zeta = x; \qquad \xi = \frac{z - E}{H},$$

which gives $\xi = 0$ at the surface and $\xi = 1$ at the base. The equations are then discretized in this new rectangular domain. The derivation formulas related to this variable change are given by *Haltiner and Williams* [1980]. In what follows we present the equations in the Cartesian reference frame (x, z) for the sake of simplicity.

To calculate the physical fields on the free surface for a given surface elevation, the dynamic conditions, (9), must be solved, together with the incompressibility condition at the free surface. The projection of (9) on the normal direction of the free surface yields for the pressure field

$$p' = \frac{1}{1 - E'^2}\left[M_{zzxx}\frac{\partial u_x}{\partial x} + M_{zzzz}\frac{\partial u_z}{\partial z} - E'^2\left(M_{xxxx}\frac{\partial u_x}{\partial x} + M_{xxzz}\frac{\partial u_z}{\partial z}\right)\right] + E \quad (20)$$

where $E' = \partial E/\partial x$. The velocity field at the free surface is obtained by combining the tangential projection with the incompressibility condition.

As already mentioned for the boundary conditions of the pressure gradient, the use of an implicit scheme forces us to consider the velocity field in (20) at time $(m+1)$. This can be done by using the expression of $\mathbf{u}^{(m+1)}$ given by (13), which, combined with the incompressibility condition, allows us to write (20) as

$$p'^{(m+1)} + \kappa\frac{\partial}{\partial x}\left(\gamma_x\frac{\partial p'^{(m+1)}}{\partial x}\right) = \kappa\frac{\partial \hat{u}_x}{\partial x} + E, \quad (21)$$

$$\kappa = \frac{1}{1 - E'^2}\left[M_{zzxx} - M_{zzzz} - E'^2\left(M_{xxxx} - M_{xxzz}\right)\right].$$

We use the same discretization method for (21) as for the pressure Poisson equation (14).

The incompressibility and the tangential dynamic equations are solved at the free surface after the calculation of the velocity field inside the domain. As a result, the surface velocities are obtained at time $(m+1)$ as a function of the velocities inside the domain of integration.

The ice thickness H is then calculated with the evolution equation (8). This equation is solved by a semi-implicit method with an Adams-Bashford scheme of second order in time

$$H_i^{(m+1)} + \frac{u_{i,1}\Delta t'}{4\Delta x}\Delta H^{(m+1)} = \frac{3}{2}G^{(m)} - \frac{1}{2}G^{(m-1)}, \quad (22)$$

$$\Delta H^{(m+1)} = H_{i+1}^{(m+1)} - H_{i-1}^{(m+1)},$$

$$G^{(m)} = H_i^{(m)} - \frac{u_{i,1}\Delta t'}{4\Delta x}\left(H_{i+1}^{(m)} - H_{i-1}^{(m)}\right) + \left(a_i - u_{z\,i,1} - u_{x\,i,1}\frac{\partial B}{\partial x}\right)^{(m)}\Delta t',$$

where $\Delta t'$ is the time step of the surface evolution. The boundary conditions for the ice thickness H are not directly imposed. In fact, these boundary values for the ice thickness are given indirectly by the boundary conditions for the horizontal velocity at the right and left sides of the domain. These velocities are calculated at each time step to satisfy the mass balance. Note that this method is directly applicable to unsteady situations where climatic parameters vary with time.

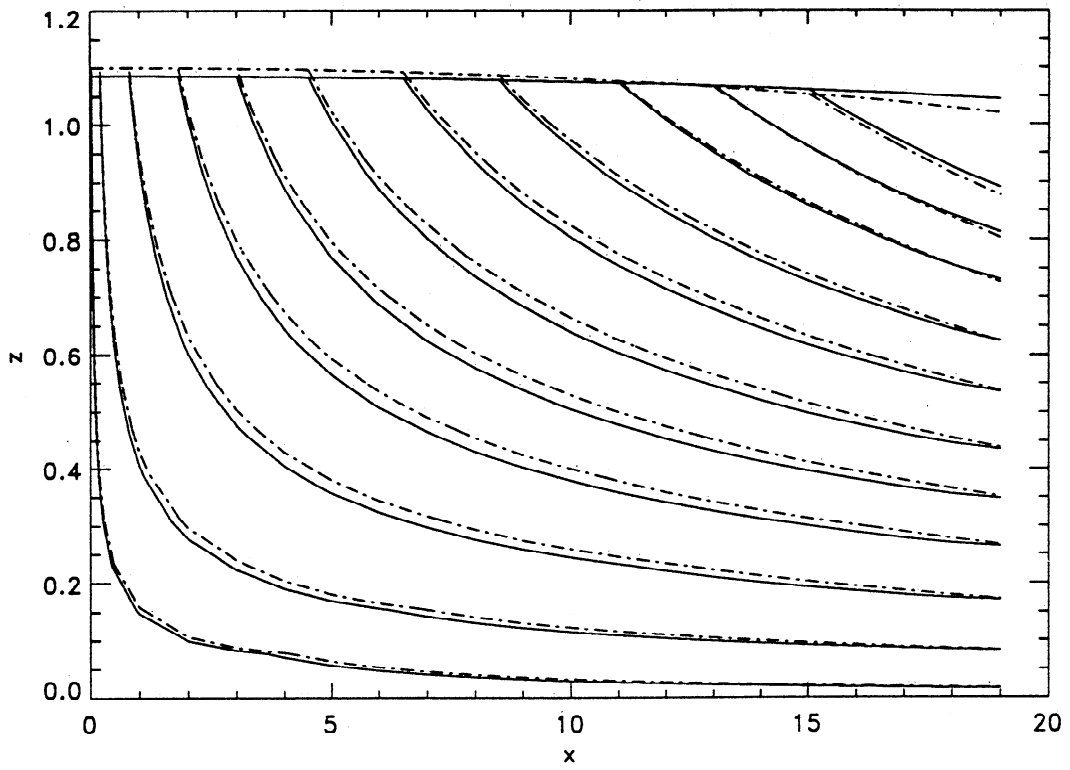

Figure 4. Flow lines and free surface elevation in the anisotropic case (solid lines) and in the isotropic case (dash-dotted lines) versus the distance from the ice divide and the depth for a flat bedrock.

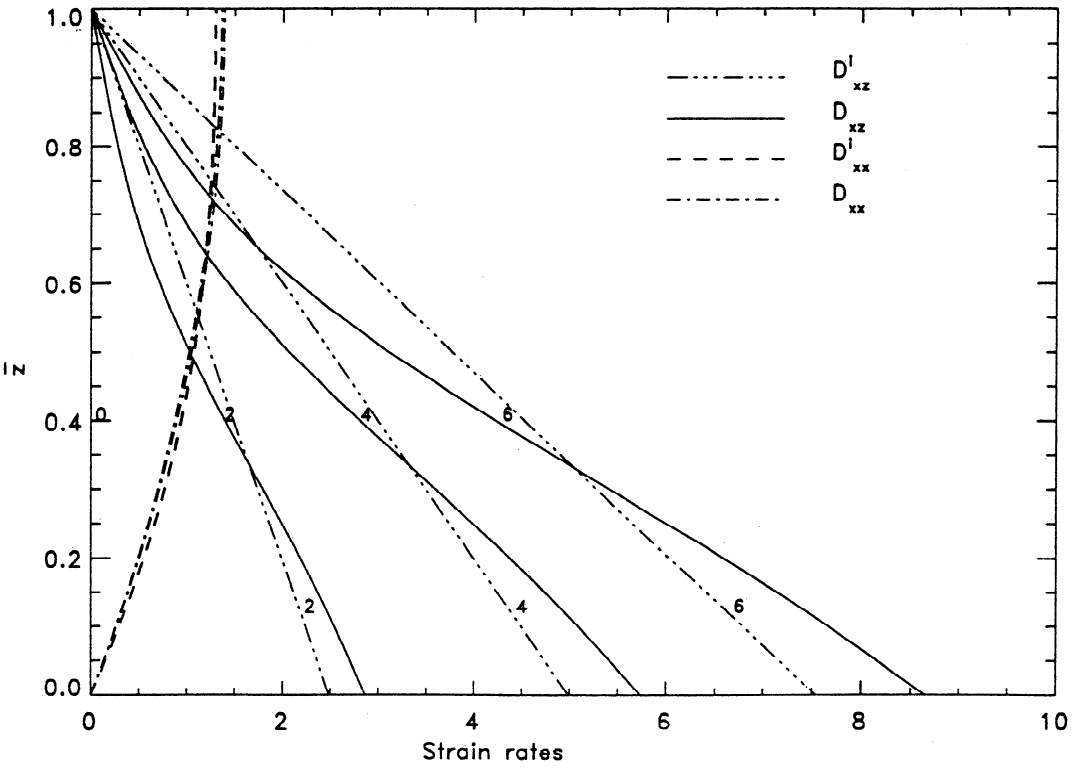

Figure 5. Shear strain rates at $x = 0, 2, 4, 6$ versus the normalized depth $\bar{z}$. The shear strain rates are represented in the anisotropic case (D_{xz}) by solid lines and in the isotropic case by dash-triple-dotted lines (D^i_{xz}). Dash-dotted lines show longitudinal strain rates at the ice divide and at $x = 6$ in the anisotropic case (D_{xx}), and dashed lines represent longitudinal strain rates at the ice divide and at $x = 6$ in the isotropic case (D^i_{xx}).

4. Results

As discussed in section 2.1, the results presented here are obtained for a given texture and Newtonian behavior.

4.1. Flat Bedrock

Mangeney et al. [1996] studied the effect of anisotropy on flow over flat bedrock with an imposed geometry. We consider here a more realistic case by introducing uneven bedrock and a supplementary degree of freedom: the surface is allowed to evolve in time to adjust to a fixed accumulation rate. The effects of anisotropy are then more complex, and we shall use the previous results to better understand these new results.

For a fixed geometry the shear strain rate is strongly influenced by anisotropy; however, when the surface elevation evolves with time, the shape of the free surface can modify the effects of the anisotropy on the shear strain rate. In fact, if we let the surface evolve, the system reacts such that the longitudinal gradient of the pressure, which (to a leading order of the shallow ice approximation) is directly related to the surface slope (see Mangeney and Califano, submitted manuscript, 1997), decreases, so that the shear strain rates are relatively low. The effect of the vertical variation of the viscosity is smoothed, partly by the decrease of the surface slope and partly by the increase of the shear strain rates. To our knowledge, no simple argument exists to predict the quantitative variations produced by this effect.

In Figure 4 we show the surface elevation and the flow lines versus the distance from the ice divide and the depth z. The free surface obtained in the anisotropic case is flatter, and the flow lines penetrate deeper into the ice sheet, becoming more horizontal when moving away from the ice divide. The decrease of the surface slope in the anisotropic case has direct consequences on the value of the basal shear stress, which, to a leading order of the shallow ice approximation, is proportional to the surface slope. The basal shear stress is then lower in the anisotropic case than in the isotropic case.

The shear strain rates in the lower part of the ice sheet are larger in the anisotropic case (see Figure 5) than in the isotropic case as was observed with a fixed geometry [*Mangeney et al.*, 1996]. However, in the upper part of the ice sheet the shear strain rates are larger in the isotropic case. The major part of the deformation occurs in the basal layers where, in the anisotropic case, the flow is globally more rapid. The effects of the anisotropy on the flow are qualitatively similar to those

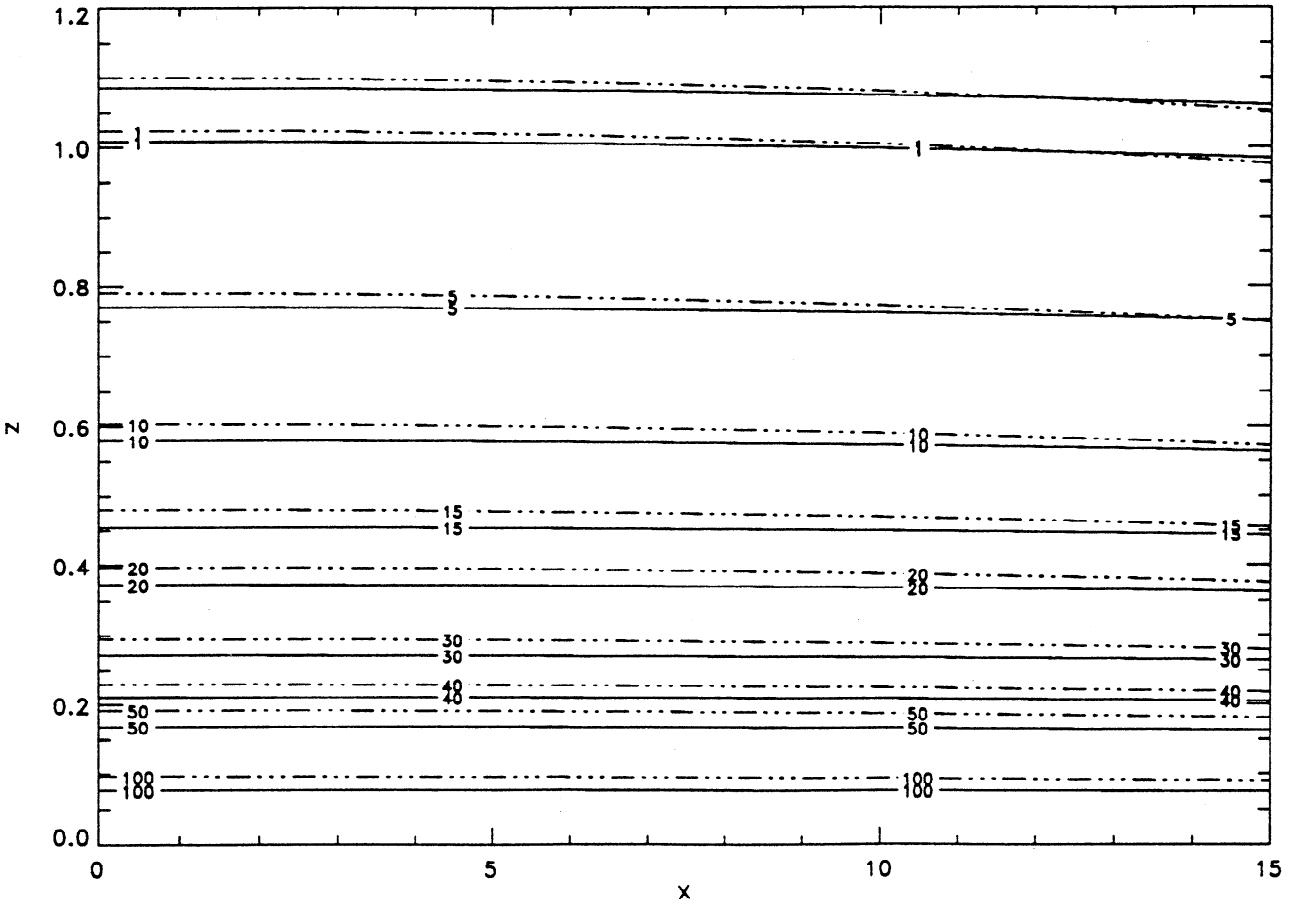

Figure 6. Isochrones in thousands of years in the isotropic case (dash-dotted lines) and in the anisotropic case (solid lines) versus the distance from the ice divide and the depth for a flat bedrock.

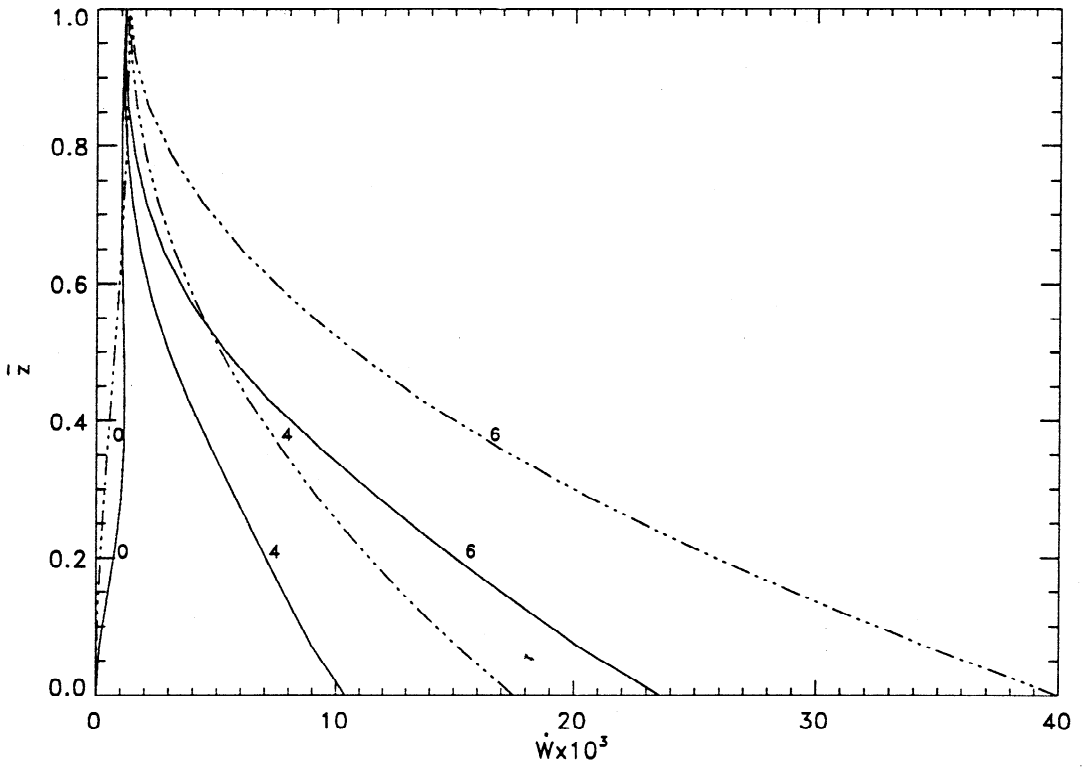

Figure 7. Vertical profiles of the viscous dissipation of heat, multiplied by 10^3, versus the normalized depth $\bar{z}$ at the ice divide (labeled 0), at $x = 4$ (labeled 4) and at $x = 6$ (labeled 6). Solid lines show the profiles in the anisotropic case, and dash-dotted lines denote the isotropic case for a flat bedrock.

observed with a fixed geometry but are quantitatively less. For example, at a distance of four ice thicknesses from the ice divide, the basal shear strain rate in the anisotropic case is 1.2 times larger than the basal shear strain rate obtained in the isotropic case (see Figure 5), while a factor of 2 was found for a fixed geometry.

Defining the region of the ice divide as a region where the shear strain rate at the base is 10 times smaller than the longitudinal strain rate at the surface, it appears that this region is smaller in the anisotropic case. In fact, this region is defined by $|x| < 9$ in the anisotropic case and by $|x| < 10.5$ in the isotropic case. A difference of two ice thicknesses was found with a fixed geometry [*Mangeney et al.*, 1996]. Because the flow in the ice divide region is essentially vertical and so the trajectory of ice particles is easy to calculate, the ice divide region was thought to be a good place for coring. This is untrue, however, when the ice divide position evolves with time. If the flow localized in the present position of the ice divide was dominated by shear strain rates in the past, the trajectory of ice particles will be difficult to calculate. This difficulty will be accentuated in the anisotropic case.

It is worth pointing out that the normalized profiles of the velocity are the same as those obtained in the case of a fixed geometry for the flow over flat bedrock. This fact can be easily understood when looking at the expression for the velocity field to leading order of the shallow ice approximation (Mangeney and Califano, submitted manuscript, 1997). At zero order the horizontal velocity of the shallow ice approximation reads

$$u(x,z) = -2\frac{\partial E}{\partial x}H^2 \int_1^{\xi} \frac{\xi}{M_{xzxz}} d\xi \qquad (23)$$

Therefore the values of the velocity normalized with respect to its value at the surface only depend on the shear viscosity M_{xzxz}.

The effect of anisotropy on the flow modifies significantly the dating of ice cores. In the anisotropic case the isochrones are flatter and the ice at a specific depth is younger (see Figure 6). Close to the bedrock, the computed age of the ice in the anisotropic case is more than 10% below the age calculated for isotropic ice.

These results would be modified by the calculation of the real, coupled, thermomechanical model. To appreciate its significance, we have calculated here only the viscous dissipation of heat, $\dot{W} = S'_{ij}D_{ij}$, which plays a key role in the heat equation. Contrary to the case of fixed geometry, the viscous dissipation of heat is smaller in the anisotropic case than in the isotropic case, except at the ice divide in the lower part of the ice sheet (see Figure 7). Incorporation of heat effects will lead to global acceleration of the flow; the larger advection of cold ice to the bottom, coupled with the diminution of the heat dissipation, should then make the basal ice colder, decreasing the concentration of shear strain rate in the

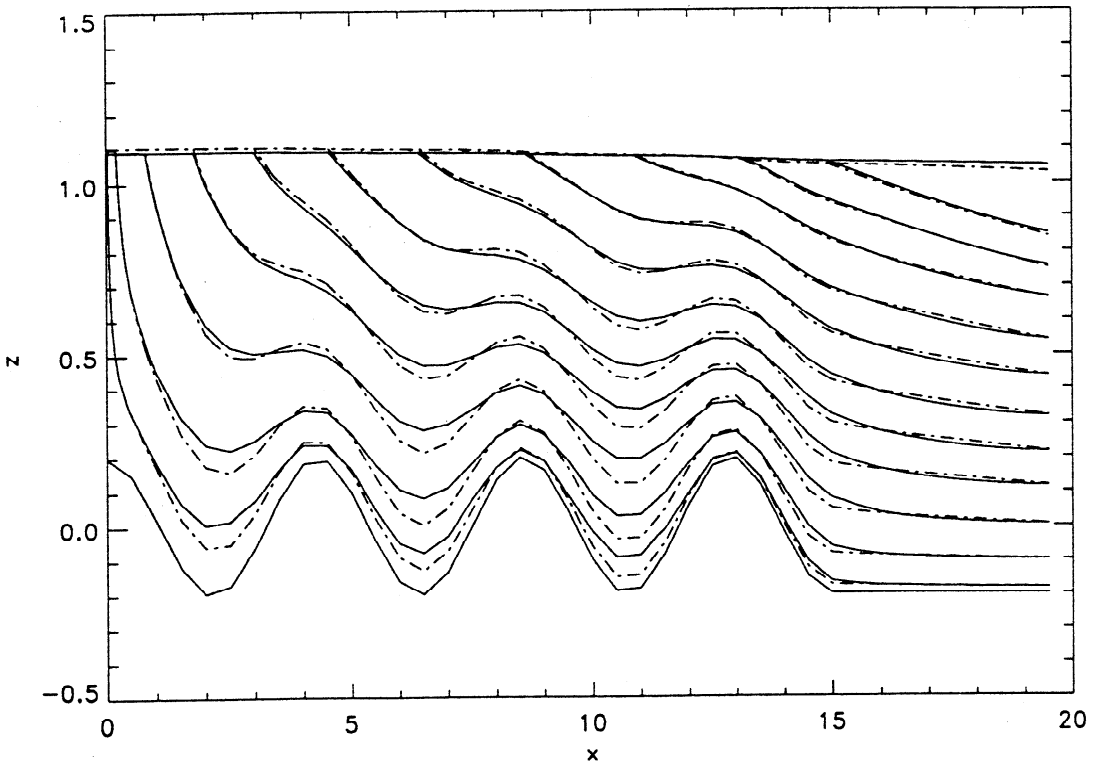

Figure 8. Flow lines and free surface elevation in the anisotropic case (solid lines) and in the isotropic case (dash-dotted lines) for $f = 7$. The line at the bottom represents the bedrock topography; the bedrock ondulations have an amplitude of 0.2 and a wavelength of approximately four ice thicknesses.

basal layers of the ice sheet. The resolution of the heat equation should then diminish the effect of anisotropy on the flow. Then, the effects of the anisotropy should influence the free surface, the temperature field, and the flow. However, we emphasize that these are only conjectures to be checked by future calculations of the thermomechanical equations.

4.2. Irregular Bedrock

Real ice sheets never flow over flat bedrock. The problem of ice sheet flow over an irregular bedrock is today very relevant: for example, at a distance of 30 km from the future European Project for Ice Coring in Antarctica (EPICA) drilling site at Dome C (Antarctica), the bedrock topography varies from -600 m to more than +800 m above sea level. This leads to a vertical variation of the bedrock topography of $\sim 50\%$ of the ice thickness over 10 km (i.e., less than four ice thicknesses).

Two questions arise. Will the anisotropy of the ice increase or decrease the effect of the bedrock topography on the flow and on the free surface? Is the preceding result, i.e., the acceleration of the flow in the anisotropic case, still valid? To study these effects, we have imposed a sinusoidal bedrock; see (10). We present here the tests for $f = 7$ and $B_0 = 0.2$, corresponding to vertical variations of the bedrock topography of 40% of the ice thickness over a distance of approximately 2 ice thicknesses. Different tests have been made with several values of amplitude B_0 and wavenumber f, leading qualitatively to the same conclusions.

In Figure 8 we show the free surface and the flow lines obtained in the isotropic case (dash-dotted lines) and in the anisotropic case (solid lines). The surface is flatter and the flow lines are less sensitive to the bedrock topography in the anisotropic case. Anisotropic ice "dives" less deeply into a hole and "climbs" less highly over a bump. The surface slope, the velocities, and all the fields are less sensitive to the bedrock topography; that is, they are more homogeneous in the horizontal direction x (see Figure 9). The anisotropic ice appears to flow over an effective bedrock less irregularly than the real bed.

A new phenomenon appears here: the partial stagnation of the ice in the holes of the bedrock. This phenomenon is easily visible when looking at the isovalues of the shear strain rate, which are shown in Figures 10a and 10b. In the isotropic case the values of the shear strain rate increase with depth everywhere along the flow line, except near the hole, where a slight slowing down of the flow occurs. In the anisotropic case the same phenomenon occurs over the bump of the bedrock, but over the holes the shear strain rate increases down to a depth of $\bar{z} \sim 0.2$ and then de-

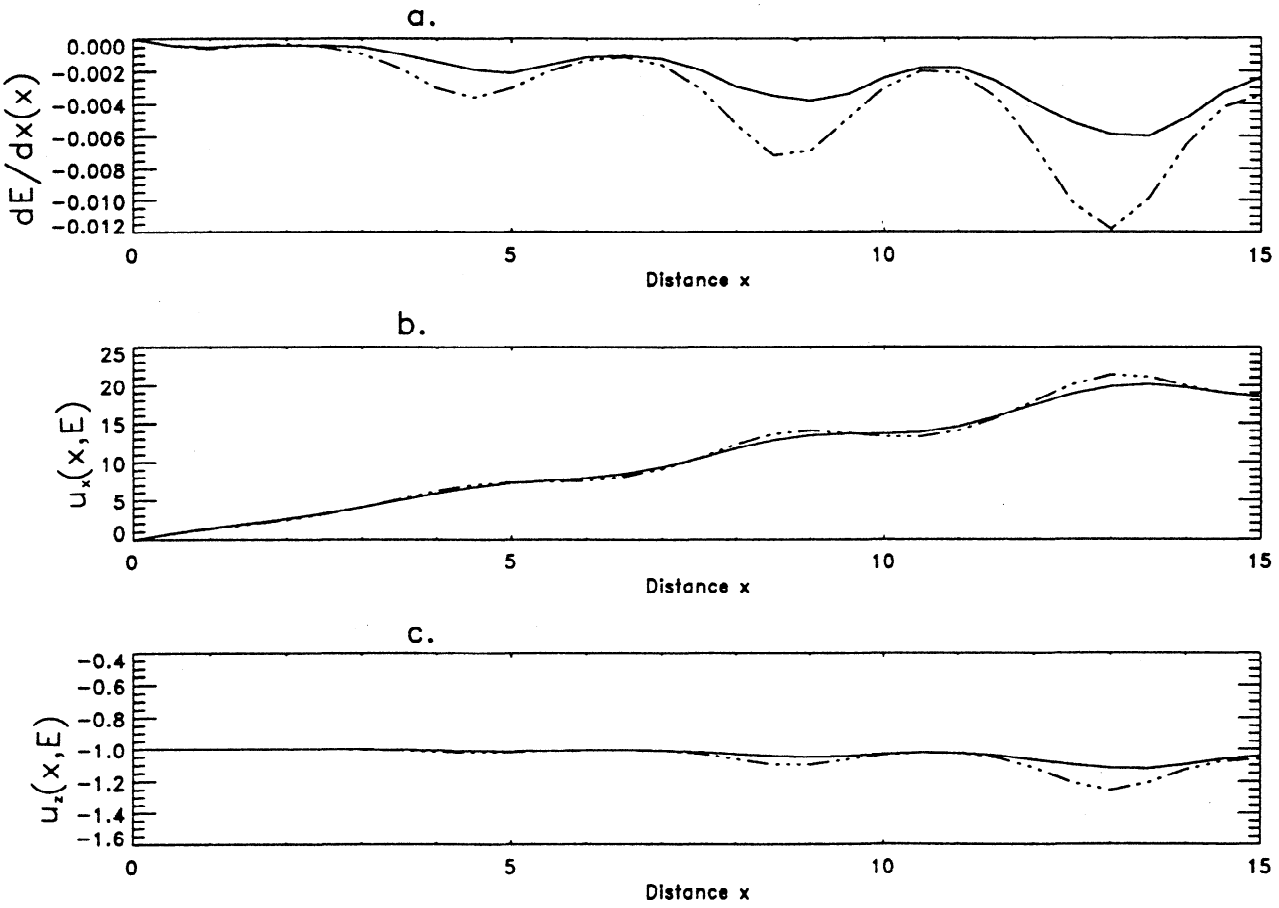

Figure 9. (a) Surface slope, (b) horizontal velocity at the surface and (c) vertical velocity at the surface versus distance from the ice divide. Solid lines represent the results in the anisotropic case, and dash-dotted lines represent the results in the isotropic case; the bedrock ondulations have an amplitude of 0.2 and a wavelength of approximately four ice thicknesses.

creases. In the isotropic case the flow lines follow the bedrock topography: ice is subjected to significant longitudinal strain rates near the bottom. However, in the anisotropic case the ice resists all longitudinal strain rates and is globally more difficult to deform. In this case a kind of boundary layer occurs near the bottom.

These effects of the anisotropy on the flow have a great influence on the dating of ice. The isochrones obtained for the anisotropic case are less sensitive to bedrock topography as observed for all the fields (see Figure 11a). If the ice is assumed isotropic, the age would be overestimated by more than 10% above the bumps of the relief and significantly underestimated (with an error of more than 100%) above the holes (see Figure 11b).

It is worth pointing out that the horizontal gradients of the longitudinal stresses in the basal layers are much higher in the anisotropic case than in the isotropic case (see Figures 10c and 10d). These gradients can reach values larger than those of the surface slope (when considering quantities without dimensions). For example, at $x = 5$ the horizontal gradient of the longitudinal stress at the base is equal to 8×10^{-4} and the surface slope is equal to 5×10^{-4} in the anisotropic case, while in the isotropic case this gradient has a value of 1.4×10^{-4} and the surface slope has a value of 1.5×10^{-3}. In the anisotropic case the horizontal gradient of the longitudinal stress is then no longer negligible with respect to the horizontal pressure gradient in the first equation of the mechanical balance (2). Over such irregular bedrock, the zeroth order of the shallow ice approximation, generally used in ice sheet modeling, is then not applicable to the flow of anisotropic ice (see Mangeney and Califano, submitted manuscript, 1997) and must be extended to at least the next nontrivial, higher-order terms.

5. Conclusions

We have shown here that to solve the complete set of mechanical equations of ice sheet flow, a careful analysis of the spatial and temporal discretization of the numerical scheme is necessary to obtain a converging solution. The use of the numerical code presented here is, however, not limited to ice sheet flow modeling. It can be applied to all materials for which linear rheolog-

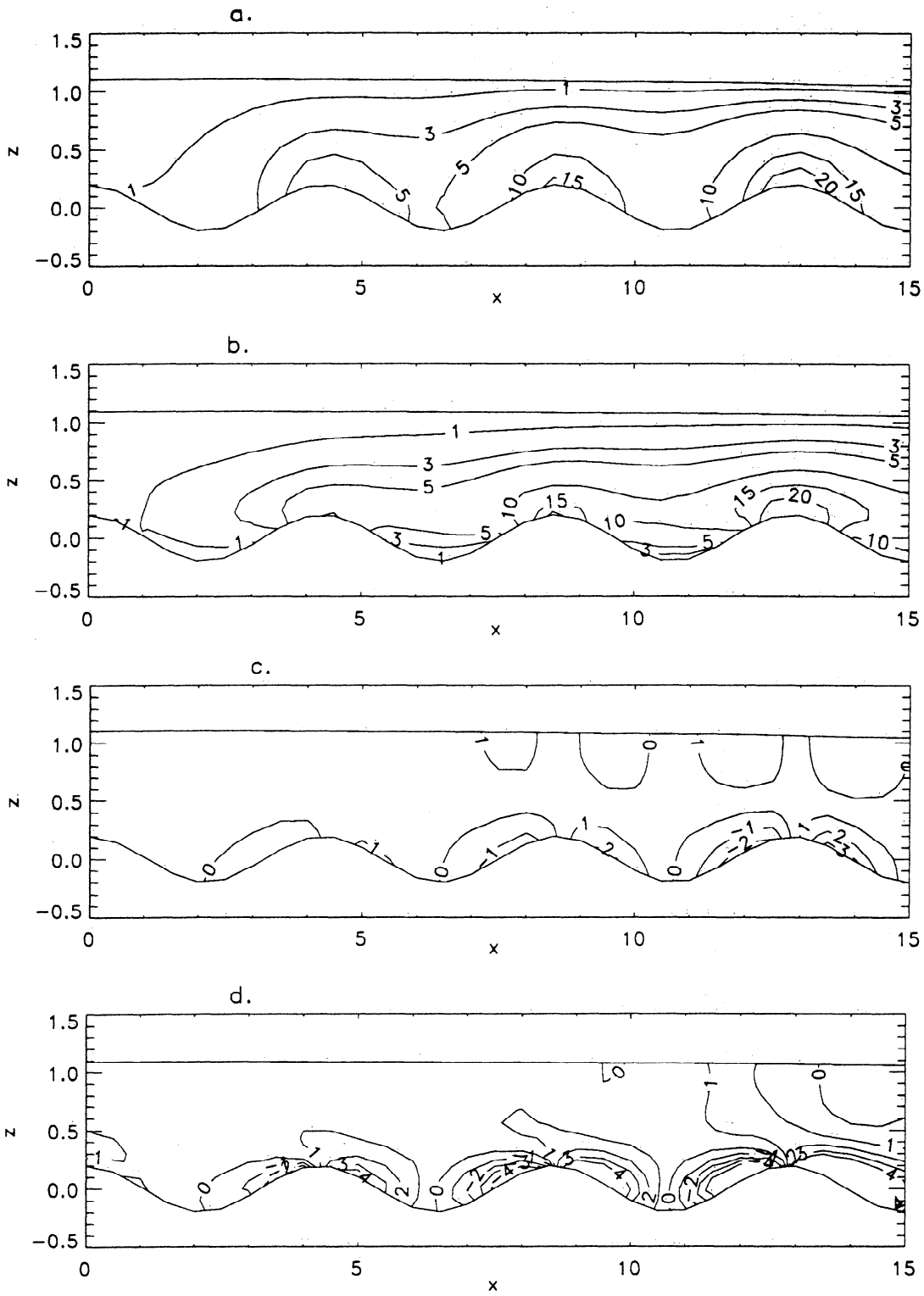

Figure 10. Isovalues of the shear strain rate D_{xz} in the (a) anisotropic case and (b) isotropic case and isovalues of the longitudinal strain rate D_{xx} in the (c) isotropic case and (d) anisotropic case versus the distance from the ice divide and the depth.

ical properties are known. It converges in all situations with very low Reynolds numbers. With slight modifications it may be used to solve transient flow, with time-dependent climatic parameters. The calculation of the transient flow can be performed using the coordinate system proposed by *Hindmarsh and Hutter* [1988], coupled to a power series of the flow near the margins [*Benney and Timson*, 1980]. The numerical code is written in primitive variables (velocity and pressure) and can be extended to three-dimensional situations.

The resolution of the heat equation, the calculation of transient flow, and the use of a more realistic flow

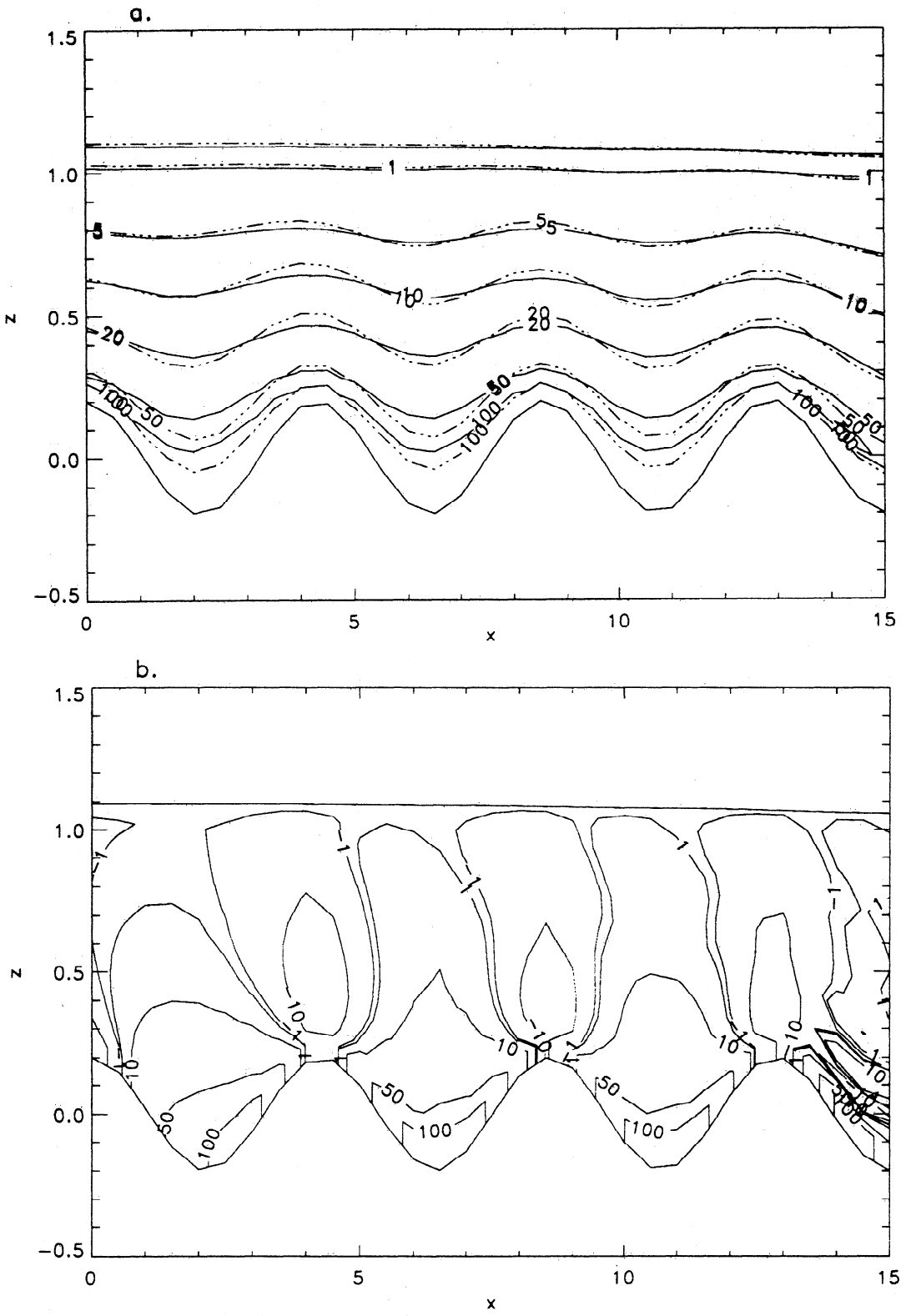

Figure 11. (a) Isochrones in thousands of years in the isotropic case (dash-dotted lines) and in the anisotropic case (solid lines). (b) Difference in percent between the calculated age for an anisotropic flow and the age calculated in the isotropic case versus the distance from the ice divide and the depth. Bedrock ondulations have an amplitude of 0.2 and a wavelength of approximately four ice thicknesses.

law are fundamental steps that must be achieved before drawing "realistic" conclusions. Here we have made a first step toward understanding the effects of anisotropy on the ice sheet flow.

The main results obtained when comparing isotropic and anisotropic flows over a flat bedrock calculated with a steady flow model under isothermal conditions and for a given texture are as follows.

1. The effects of anisotropy are partly smoothed out by the deformation of the free surface which is flatter and by the shear strain rates which are larger and more concentrated near the bedrock in the anisotropic case than in the isotropic case.

2. The flow is globally faster in the anisotropic case, but it is less than the flow obtained when a fixed geometry is imposed.

3. The ice divide region, where the longitudinal strain rates are significant, is less extensive in the anisotropic case than in the isotropic case.

4. The isochrones are flatter in the anisotropic case, and anisotropic ice at fixed depth is younger than isotropic ice, by more than 10% in the basal layers.

When irregular bedrock is considered in the anisotropic case, we observe that (1) the flow is less sensitive to the variations of bedrock topography than in the isotropic case; (2) the fields and the isochrones in the horizontal direction x are more homogeneous than in the isotropic case; (3) the flow is faster above the bumps, and the ice is stagnant in the holes of the bedrock; and (4) above the bumps the ice is younger by more than 10% compared with the isotropic ice, and in the holes of the relief it is older by more than 100%.

These results are obtained with a fixed texture and without recrystallization layers at the base of the ice sheet. The presence of recrystallization processes leads to a layer of isotropic ice near the bedrock of several hundred meters. The presence of this layer will certainly decrease the phenomenon of stagnation of the ice within the holes of the relief. For the time being, it is not known whether this phenomenon will remain if the evolution of the texture is taken into account.

We have shown that surface elevation, flow, and dating are very sensitive to the texture distribution in the ice sheets. Consideration of anisotropy effects will change the values of rheological and climatic parameters that are determined by inverse models using surface elevation measurements [*Remy et al.*, 1996] or the position of isochrones, where the age is known [*Dahl-Jensen et al.*, 1993].

It is evident that the effects of anisotropy have significant practical consequences since they change the dating of ice cores. In particular, consideration of these effects may have a major impact on the choice of drilling locations.

Acknowledgments. This work was supported by the Programme National d'Etude du Climat (PNEDC), the environment program of the CCE (in France), and the EISMINT program (European Science Foundation). We are grateful to L. Lliboutry for fruitful discussions. We thank the Observatoire de Meudon for their facilities.

References

Abdallah, S., Numerical solutions for the pressure Poisson equation with Neumann boundary conditions using a non-staggered grid, I, *J. Comput. Phys.*, *70*, 182-192, 1987a.

Abdallah, S., Numerical solutions for the incompressible Navier-Stokes equations in primitive variables using a non-staggered grid, II, *J. Comput. Phys.*, *70*, 193-202, 1987b.

Alley, R. B., Flow-law hypotheses for ice sheet modeling, *J. Glaciol.*, *38*(129), 245-256, 1992.

Azuma, N., A flow law for anisotropic ice and its application to ice sheets, *Earth Planet. Sci. Lett.*, *128*, 601-614, 1994.

Beaudoin, A. J., P. R. Dawson, K. K. Mathur, U. F. Kocks, and D. A. Korzelwa, Application of polycristal plasticity to sheet forming, *Comput. Methods Appl. Mech. Eng.*, *117*, 49-70, 1994.

Benney, D. J., and W. J. Timson, The rolling motion of a viscous fluid on and off a rigid surface, *Stud. Appl. Math.*, *63*, 93-98, 1980.

Castelnau, O., Modelisation du comportement mecanique de la glace polycristalline par une approche auto-coherente; application du developpement de textures dans les glaces des calottes polaires, thesis, Univ. Joseph Fourier, Grenoble, France, 1996.

Castelnau, O., P. Duval, R. A. Lebensohn, and G. R. Canova, Viscoplastic modeling of texture development in polycrystalline ice with a self-consistent approach: Comparison with bound estimates, *J. Geophys. Res.*, *101*, 13,851-13,868, 1996.

Castelnau, O., G. R. Canova, R. A. Lebensohn, and P. Duval, Modeling viscoplastic behavior of anisotropic, polycristalline ice with a self-consistent approach, *Acta Mater.*, in press, 1997.

Chorin, A. J., A numerical method for solving incompressible viscous flow problems, *J. Comput. Phys.*, *2*, 12-26, 1967.

Dahl-Jensen, D., S. J. Johnson, C. U. Hammer, H. B. Clausen, and J. Jouzel, Past accumulation rates derived from observed annual layers in the GRIP ice core from Summit, Central Greenland, in *Ice in Climite System*, edited by W. R. Peltier, pp. 517-532, Springer-Verlag, New York, 1993.

Deville, M. O., An alternating direction implicit algorithm for viscous free surface flows, *J. Meca.*, *14*(1), 161-187, 1975.

Doake, C. S. M., and E. W. Wolff, Flow law for ice in polar ice sheets, *Nature*, *314*(6008), 255-257, 1985.

Duval, P., and O. Castelnau, Dynamic recristallization of ice in polar ice sheets, *J. Phys. IV*, *5*, 197-205, 1995.

Firestone, J., E. D. Waddington, and J. Cunningham, The potential for basal melting under Summit, Greenland, *J. Glaciol.*, *36*(123), 163-168, 1990.

Fortin, M., R. Peyret, and R. Temam, Resolution numerique des equations de Navier-Stokes, *J. Meca.*, *10*(3), 357-390, 1971.

Fowler, A. C., and D. A. Larson, The uniqueness of steady state flows of glaciers and ice sheets, *Geophys. J. R. Astron. Soc.*, *63*, 333-345, 1980.

Haltiner, G. J., and R. T. Williams, *Numerical Prediction and Dynamic Meteorology*, John Wiley, New York, 1980.

Harlow, F. H., and J. E. Welch, Numerical calculation of time-dependent viscous incompressible flow of fluid with free surface, *Phys. Fluids*, *8*, 2182-2189, 1965.

Hindmarsh, R. C., and K. Hutter, Numerical fixed domain mapping solution of free surface flows coupled with an evolving interior field, *Int. J. Numer. Anal. Methods Geomech.*, *12*, 437-459, 1988.

Hooke, R. L., Flow law for polycrystalline ice in glaciers: Comparison of theoretical predictions, laboratory data, and field measurements, *Rev. Geophys.*, *19*(4), 664-672, 1981.

Hutter, K., F. Legerer, and U. Spring, First-order stresses and deformations in glaciers and ice sheets, *J. Glaciol.*, *27*(96), 227-270, 1981.

Hutter, K., Thermo-mechanically coupled ice-sheet response-cold, polythermal, temperate, *J. Glaciol.*, *39*(131), 65-86, 1993.

Jenssen, D., A three dimensional polar ice sheet model, *J. Glaciol.*, *18*(8), 373-389, 1977.

Lliboutry, L., Anisotropic, transversally isotropic nonlinear viscosity of rock ice and rheological parameters inferred from homogenization, *Int. J. Plasticity*, *9*, 619-632, 1993.

Mangeney, A., Modelisation de l'ecoulement de la glace dans les calottes polaires: Prise en compte d'une loi de comportement anisotrope, thesis, Univ. Pierre et Marie Curie, Paris, 1996.

Mangeney, A., F. Califano, and O. Castelnau, Isothermal flow of an anisotropic ice sheet in the vicinity of an ice divide, *J. Geophys. Res., 101*, 28,189-28,204, 1996.

Morton, K. W., Stability and convergence in fluid flow problems, *Proc. R. Soc. London A*, *323*, 237-253, 1971.

Nye, J. F., The mechanics of glacier flow, *J. Glaciol.*, *2*(12), 82-93, 1952.

Nye, J. F., The distribution of stress and velocity in glaciers and ice-sheets, *Proc. R. Soc. London A*, *239*, 113-133, 1957.

Paterson, W. S. B., and E. D. Waddington, Past precipitation rates derived from ice core measurements: Methods and data analysis, *Rev. of Geophys.*, *22*(2), 123-130, 1984.

Peyret, R., and T. D. Taylor, *Computational Methods in Fluid Flows*, Springer-Verlag, New York, 1983.

Phillips, N. A., A coordinate system having some special avantages for numerical forecasting. *J. Meteorol.*, *14*(2), 184-185, 1957.

Pimienta, P., and P. Duval, Rate controlling processes in the creep of polar ice, *J. Phys. C Solid State Phys.*, *48*, suppl. 3, 243-248, 1987.

Pracht, W. E., A numerical method for calculating transient creep flows, *J. Comput. Phys.*, *7*, 46-60, 1971.

Raymond, C. F., Deformation in the vicinity of ice divides, *J. Glaciol.*, *29*(103), 357-73, 1983.

Remy, F., C. Ritz, and L. Brisset, Ice sheet flow features and rheological parameters derived from precise altimetric topography, *Ann. Glaciol.*, *23*, 277-284, 1996.

Schott Hvidberg, C. , A thermo-mechanical ice flow model for the center of large ice sheets, Ph.D. dissertation, Univ. of Copenhagen, Copenhagen, 1993.

Schott Hvidberg, C., Steady state thermo-mechanical modelling of ice flow near the center of large ice sheets with the finite element technique, *Ann. Glaciol.*, *23*, 116-124, 1996.

Sotiropoulos, F., and S. Abdallah, The discrete continuity equation in primitive variable solutions of incompressible flow, *J. Comput. Phys.*, *95*, 212-227, 1991.

Svendsen, B., and K. Hutter, A continuum approach to model induced anisotropy in glaciers and ice sheets, *Ann. Glaciol.*, *23*, 262-270, 1996.

Thorsteinsson, T., J. Kipfsuhl, and H. Miller, Textures and fabrics in the GRIP ice core, *J. Geophys. Res.*, in press, 1997.

Van der Veen, C. J., and I. M. Whillans, Development of fabric in ice, *Cold Reg. Sci. Technol.*, *22*, 171-195, 1994.

F. Califano, Scuola Normale Superiore, Piazza dei Cavalieri 7, 56100, Pisa, Italy. (e-mail: califano@cibs.sns.it)

K. Hutter, Institut fur Mechanik, Hochschulstrasse 1, D-64289 Darmstadt, Germany. (e-mail: hutter@mechanik.th-darmstadt.de)

A. Mangeney, Observatoire de Paris-Meudon, 5 Place J. Janssen, 92195 Meudon Cedex, France. (e-mail: mangeney@megasg.obspm.fr)

(Received October 4, 1996; revised May 29, 1997; accepted June 6, 1997.)